

Local Tomography in 3-D SPECT

Eric Todd Quinto, Tania Bakhos, and Sohhyun Chung

ABSTRACT. We present slant-hole SPECT and describe the microlocal analysis of the SPECT operator. We present three Lambda type local reconstruction methods, and we analyze how singularities are added to reconstructions using each method. We demonstrate how one method adds weaker singularities than the others in reconstructions and we give the microlocal analysis of the forward operator.

1. Introduction and Notation

Single Photon Emission Computed Tomography (SPECT) is a diagnostic medical modality to detect metabolic processes or body structure. The physical resolution is not usually as good as with X-ray tomography, but it can be useful to detect metabolic processes. These maps of metabolic processes are used to pinpoint tumors, which absorb nutrients faster than the surrounding tissue and in epilepsy research to map activities in the brain when someone has a seizure.

A patient ingests a nutrient with a radioactive tracer attached. The SPECT scanner measures the emissions from the body in a range of directions, and a tomography algorithm determines where the nutrients are located. Detectors are collimated to detect only the emissions that are on fixed lines. For each line, the data collected represents the number

Key words and phrases. Emission Tomography, Radon Transforms, Microlocal Analysis.

The first author was supported in part by NSF Grant DMS 0456858, and the second author was supported by an REU from this grant. The third author was supported by the Tufts University Summer Scholars Program. The first author thanks Larry Shepp, Frank Natterer, Adel Faridani, and Alfred Louis for stimulating mathematical discussions over the years and for pointing out the importance of the ideas in Remark 4.14. The authors thank the referee for helpful comments including suggestions that make Section 4 clearer.

of emissions from points on that line in the direction of the detector. In standard SPECT, the detector array moves around the body and takes data over lines with directions perpendicular the axis of rotation. This is a time consuming process because the heavy detector array has to physically move around the body. Slant-Hole SPECT is a novel data acquisition method in which the circular detector array rotates about its center, and the array itself does not need to be moved around the patient. This means that a full data set for this specific geometry can be acquired more quickly than for standard data [50]. Several algorithms for slant-hole SPECT have been developed [31, 50] if one has full data, but, to the author's knowledge, there is no algorithm for local data except the one presented here. In Section 3, we explain practical reasons why local algorithms are needed.

The article is organized as followed. In Section 2, we describe X-ray computed tomography then the basic model for SPECT. We also develop the notation for the article. In Section 3, we introduce the geometry and mathematics for SPECT and present three basic algorithms for slant-hole SPECT. We discuss singularities and wavefront sets in Section 4, and in the appendix, we give the proofs of the microlocal results.

2. The models for X-ray Computerized Tomography and SPECT

We consider three-dimensional tomographic data over parallel lines. So, we consider the *parallel-beam parameterization* of lines in space. To specify lines, we provide the direction of the line and a point on the line. Let $\theta \in S^2$ and let

$$\theta^\perp = \{y \in \mathbb{R}^3 \mid y \cdot \theta = 0\}$$

be the plane through the origin perpendicular to θ . For $\theta \in S^2$ and $y \in \theta^\perp$, we denote the line through y in direction θ by

$$L(y, \theta) = \{y + t\theta \mid t \in \mathbb{R}\}.$$

This allows us to parameterize all the lines in space by the set

$$Y = \{(y, \theta) \mid \theta \in S^2, y \in \theta^\perp\}. \quad (2.1)$$

Beer's law dictates how radiation is attenuated as it passes through the body. We denote the *attenuation coefficient (or absorption)* of the body at point x by $\mu(x)$. Although μ depends on frequency of the radiation, for monochromatic radiation, $\mu(x)$ is proportional to the density of the body at x . Denote the intensity of radiation at x by $f(x)$ and assume the emitter of X-rays is at the point x_0 on a line L and the detector is at

$x_1 \in L$. According to Beer's Law,

$$\frac{df}{dx} = -\mu(x)f(x)$$

where d/dx is the derivative along the line in the direction of the detector. It is very easy to integrate this separable differential equation, and the result is

$$\frac{f(x_1)}{f(x_0)} = \exp\left(-\int_{x_0}^{x_1} \mu(x)dx\right). \quad (2.2)$$

That is, knowing $f(x_0)$ and $f(x_1)$ one can measure the line integral of μ from x_0 to x_1 along L . We assume x_1 is outside the convex hull of the body and the detector is at x_1 and is collimated along the ray from x_0 to x_1 . Then this integral is the *divergent beam transform* of μ from source x_0 in direction θ :

$$D_{x_0}\mu(\theta) := \int_{s=0}^{\infty} \mu(x_0 + s\theta) ds.$$

We can now rewrite (2.2) to become

$$f(x_1) = \exp(-D_{x_0}\mu(\theta))f(x_0). \quad (2.3)$$

In X-ray tomography, x_0 is the source of X-rays and it is on one side of the body and x_1 is the detector on the other side.

In *Single Photon Emission Computed Tomography (SPECT)*, the patient ingests a radioactive substance with a nutrient (sugar, etc.) attached. The goal is to find the locations where the nutrient collects by counting emissions. We assume that $\mu(x)$, the attenuation coefficient of the body at x , is known, and we let $f(x)$ be the concentration of radioactive emitters at x . Collimated detectors are placed around the body and emissions are counted along the collimated lines to the detectors. Assume a detector is collimated in direction θ to detect data on $L(y, \theta)$ (i.e., the detector is in the θ direction from the body along $L(y, \theta)$).

According to Beer's law, emissions from $x_0 \in L(y, \theta)$ at the detector is given by (2.3), so the total emissions along $L(y, \theta)$ are just the integral of (2.3) over $x_0 \in L(y, \theta)$. This transform is called the *Attenuated Radon Transform* and, if $d\ell(x)$ is the measure on the line $L(y, \theta)$, it is

$$\begin{aligned} R_\mu f(y, \theta) &:= \int_{x \in L(y, \theta)} f(x) \exp\left(-\int_{s=0}^{\infty} \mu(x + s\theta) ds\right) d\ell(x) \\ &= \int_{t=-\infty}^{\infty} f(y + t\theta) \exp\left(-\int_{s=t}^{\infty} \mu(y + s\theta) ds\right) dt. \end{aligned} \quad (2.4)$$

This is a complicated transform, and a simplifying assumption is often made. One assumes the attenuation is some constant, ν , in a convex region of the body including the emitters, $\text{supp } f$. After multiplying the data by a known factor depending on the shape of the convex set on which μ is constant, we get the ***Exponential Radon transform***:

$$E_\nu f(y, \theta) := \int_{t=-\infty}^{\infty} f(y + t\theta) e^{\nu t} dt, \quad P := E_0. \quad (2.5)$$

This reduction is derived, for example, in [29, 3]. We call $P = E_0$ the *parallel beam transform*. We assume that we know ν and are trying only to find f .

In *standard SPECT*, the detectors are collimated to a set of parallel lines that are perpendicular to the axis of rotation, and the detector array rotates around that axis. In this case, the lines are all in parallel planes, and the problem can be viewed as a planar problem.

Much beautiful mathematics has been created in attempts to invert the planar attenuated transform. In 1980, Tretiak and Metz [48] proved a filtered back projection type inversion formula for the much simpler exponential transform. Markoe [33] developed a Fourier reconstruction method for this transform. Using integral equation techniques Quinto was able to prove injectivity for the class of rotation invariant Radon transforms (which includes the exponential transform) [43]. Motivated by his result, Quinto hoped that one could prove injectivity for not only the attenuated transform (with smooth μ) but also for any Radon line transform with smooth positive weight (see (A.4)). However, in the mid-1980s, Jan Boman gave a beautiful counterexample to injectivity for a smooth positive weight [4]. At around the same time Finch showed in an elegant article [11] that the general attenuated transform was injective as long as the attenuation, μ was bounded in relation to the support of f (the exact condition is $\|\mu\|_\infty \text{diam}(\Omega) < 5.37$). He used clever energy estimates inspired by work Mukhometov from the 1970s [34]. Derevtsov, Dietz, Schuster, and Louis test best approximation and approximate inverse on two dimensional SPECT in [7]. This transform was not inverted until 2002 with beautiful ground-breaking work of Bukhgeim [2] and Novikov [39], and these formulas were implemented in [18, 30, 36].

The question of how to find both μ and f , is even more difficult. For the exponential transform, one can show that, as long as f is not radial, then one can reconstruct both ν and f from $E_\nu f$ [47]. Natterer discovered necessary range conditions for the general attenuated transform (e.g., [37]), and he used these in very clever ways to find μ under the assumption that $\text{supp } f$ is a finite set [35]. One can read about these developments in [29, 10].

Now, we leave planar SPECT. Our goal is to explore a new 3-D data acquisition geometry.

3. Slant-Hole SPECT

Slant-hole SPECT involves a new data acquisition geometry in which the collimated detectors are slanted at an angle of $\phi \in (0, \pi/2)$ from a vertical axis at the center of the detector array. The array rotates around this center to collect data. The resulting set of lines all are at angle ϕ from this vertical axis, so they are parallel any cone with opening angle ϕ from the vertical axis. As can be guessed from Figure 1, data acquisition is faster [50] with slant-hole SPECT than standard SPECT, since the detector array does not have to be moved all around the patient. It just needs to be rotated about its axis. In Section 4 we will explain that some singularities of f are not detected from this data. So, sometimes the detector array is rotated to a second position so as to get more complete data. Bakhos tested this for the data set of Figure 2 with excellent results [3].

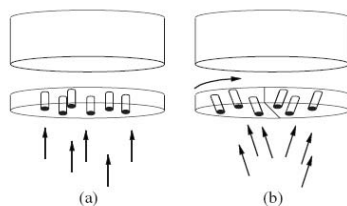


FIGURE 1. (a): Detector array for standard SPECT. To collect data, the entire array rotates about an axis through the body that is perpendicular to the direction of the collimators. (b): Detector array for slant-hole SPECT. To collect data, the array stays at the same position in space and just rotates about its center.

Since slant-hole SPECT is so much newer than standard SPECT, much less is known. For the exponential transform, Kunyansky[31] and Wagner, Noo, and Clackodyle [50] have developed clever inversion methods if all data are given. For the parallel beam transform ($\nu = 0$) Orlov [40] developed an inversion method using the projection slice theorem. We will discuss this in Remark 4.10.

The author knows of no inversion method for the general attenuated transform and slant-hole data. In beautiful work, Greenleaf and Uhlmann

[16, 17] developed the microlocal analysis of more general X-ray transforms on so-called admissible line complexes on manifolds, and the sets of lines we consider are special cases. Boman and Quinto [5] studied the microlocal analysis for X-ray transforms on admissible line complexes in \mathbb{R}^3 including the sets of lines we study here.

Another important limitation of slant-hole SPECT is the fact that, to image all of a cross-section of the torso, the detector array has to be very large. To see this, assume $\phi = \pi/4$ and the torso is 40 cm wide and the detector array is 30 cm above the center of the body. Then the array has to have diameter 100 cm. in order that lines from the edge of the body at angle $\pi/4$ reach the array if the detector is like the one in Figure 1.

This issue also explains why region of interest algorithms are practically important. In region of interest tomography, the goal is to reconstruct a smaller region in the body. In slant-hole SPECT, a smaller array could be used than for the entire torso. With the geometry given above, the detector would have diameter the diameter of the region of interest plus 60 cm. Also, the current algorithms for slant-hole SPECT [31, 50] require all data through the body, and that would require an even larger detector.

Now we introduce the mathematical notation needed to solve our problem.

DEFINITION 3.1. Let $\phi \in (0, \pi/2)$. We let \mathfrak{C}_ϕ be the vertical cone through the origin with angle ϕ from the z -axis. We let $C_\phi = \mathfrak{C}_\phi \cap S^2$. Then, C_ϕ is a latitude circle on S^2 . We define

$$Y_\phi = \{(y, \theta) \mid \theta \in C_\phi, y \in \theta^\perp\} \quad (3.1)$$

and call Y_ϕ the *slant-hole SPECT line complex*.

Y_ϕ is the set of lines in the slant-hole SPECT data set and the set of lines in Y_ϕ are parallel the cone \mathfrak{C}_ϕ . Equivalently, they have directions on the latitude circle C_ϕ .

This setup can be made more general by considering different curves of directions on S^2 . Let C be a smooth regular curve on S^2 and then we can consider

$$Y_C = \{(y, \theta) \mid \theta \in C, y \in \theta^\perp\} \quad (3.2)$$

the set of lines in directions parallel directions on C . The analysis and reconstruction operators presented here are valid in this more general setting as shown in Theorem A.1 and [46].

Let $x \in \mathbb{R}^3$, then $x - (x \cdot \theta)\theta$ is the projection of x onto θ^\perp . The dual operator to E_ν on the complex Y_ϕ is called the *backprojection operator*

and it is defined for $g \in C(Y_\phi)$ as

$$E_\nu^* g(x) := \int_{\theta \in C_\phi} e^{\nu x \cdot \theta} g(x - (x \cdot \theta)\theta, \theta) d\theta. \quad (3.3)$$

It is the weighted average of g over all lines through x . Similar formulas are valid if C is an arbitrary differentiable, regular curve on S^2 as is discussed in [46].

3.1. Basic Backprojection. A natural and very simple reconstruction method is just to compose E_ν and its dual. The analogous algorithm was one of the earliest reconstruction methods in X-ray tomography. However, for E_ν , it is better to compose with $E_{-\nu}^*$.

THEOREM 3.2. *Let $f \in C_c(\mathbb{R}^3)$. Then,*

$$E_{-\nu}^* E_\nu f(x) = \int_{y \in \mathfrak{C}_\phi} \frac{f(x+y)}{\|y\|} e^{\nu s} \Big|_{y=s\theta} dy. \quad (3.4)$$

Coauthors Sohhyun (Holly) Chung [6] and Tania Bakhos [3] showed that the composition of $E_\nu^* E_\nu$ is more complicated and has a somewhat worse kernel than $E_{-\nu}^* E_\nu$. Bakhos and Chung discovered and then proved the properties of the operators we will soon define (e.g., (3.7)). They both made rigorous tests of the algorithms, and some of their reconstructions will be presented here.

PROOF. The proof of Theorem 3.2 is a simple calculation. We start with the definitions and then rearrange terms.

$$\begin{aligned} E_{-\nu}^* E_\nu f(x) &= \int_{\theta \in C} e^{-\nu x \cdot \theta} \int_{-\infty}^{\infty} f(x - (x \cdot \theta)\theta + t\theta) e^{\nu t} dt d\theta \\ &= \int_{\theta \in C} e^{-\nu x \cdot \theta} \int_{-\infty}^{\infty} f(x + (t - (x \cdot \theta))\theta) e^{\nu t} dt d\theta \end{aligned}$$

Now, let $s = t - (x \cdot \theta)$ so $t = s + (x \cdot \theta)$, and we get

$$E_{-\nu}^* E_\nu f(x) = \int_{\theta \in C} \int_{-\infty}^{\infty} f(x + s\theta) e^{\nu s} ds d\theta$$

Next, we note that the measure on the cone \mathfrak{C}_ϕ is $dy = |s| ds d\theta$ so

$$\begin{aligned} E_{-\nu}^* E_\nu f(x) &= \int_{\theta \in C_\phi} \int_{s \in \mathbb{R}} f(x + s\theta) e^{\nu s} ds d\theta \\ &= \int_{y \in \mathfrak{C}_\phi} \frac{f(x+y)}{\|y\|} e^{\nu s} \Big|_{y=s\theta} dy \end{aligned} \quad (3.5)$$

□

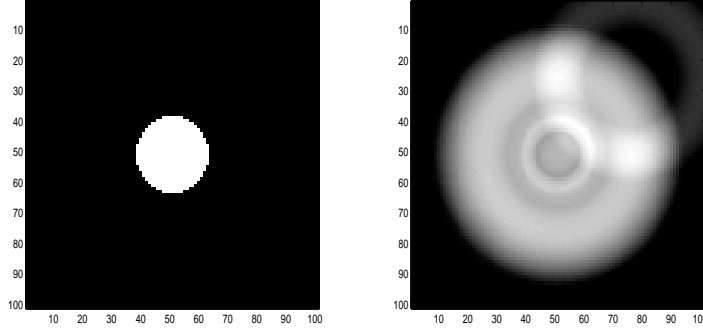


FIGURE 2. Cross-section with the $x - y$ plane of phantom (left) and backprojection reconstruction (right) of disks with center $(0,0,0)$ radius $1/2$, center $(0,0,1)$ radius $1/2$ center $(1,1,1)$ radius $1/4$ center $(-1,-1,-1/2)$ radius $1/4$. The disks above the $x - y$ -plane have density two and the others have density one. The angle with the z -axis $\phi = \pi/4$. The center of the figure is the origin and the range in x and y is from -2 to 2 .

Note that in (3.4), the integral of $f(x + \cdot)$ over the cone \mathfrak{C}_ϕ ; values of f near x are emphasized *as well as* values of f on the cone above x (when $s \gg 0$)!

Obviously, the reconstructions in Figure 2 is interesting but not acceptable. A better idea is to use some sort of derivative sharpening, as in planar Lambda CT, before backprojecting.

3.2. Planar Lambda CT. We will now briefly review Lambda tomography, an elegant local reconstruction method for the X-ray transform in the plane. For $f \in C_c(\mathbb{R}^2)$, we let

$$Pf(y, \theta) := \int_{t=-\infty}^{\infty} f(y + t\theta) dt$$

where $\theta \in S^1$ and $y \in \theta^\perp = \{z \in \mathbb{R}^2 \mid z \cdot \theta = 0\}$ is the line through the origin perpendicular to θ . The transform P is, of course, the planar analogue of the parallel beam transform E_0 .

For planar X-ray CT, filtered back projection gives $f = \frac{1}{4\pi} P^* \Lambda_y P f$ where $\Lambda_y = \sqrt{-d^2/dy^2}$ [38]. Here d/dy is the derivative in the direction $\pi/2$ units in the counterclockwise direction from θ in the line θ^\perp .

Lambda X-ray Tomography [8, 49] replaces the non-local operator $\Lambda_y = \sqrt{-d^2/dy^2}$ by the second derivative

$$\Lambda_x f(x) = P^* \frac{-d^2}{dy^2} P f(x). \quad (3.6)$$

This operator is local in the sense that one needs only values of Pf on lines near x to calculate $P^* \frac{-d^2}{dy^2} P f(x)$, since P^* integrates over lines through x , and to calculate the derivative $\frac{-d^2}{dy^2} P f$, one needs only data over lines near x . The result is a local operator, and it reconstructs singularities (e.g., boundaries) not density values. Λ_x is an elliptic pseudodifferential operator since it is a multiple of $\sqrt{-\Delta}$. An important addition that Kennan Smith originally suggested [9] is to add a factor of $P^* P f$ to provide contour. The resulting transform is $P^* (-(d^2/dy^2) + k) P f$. This was thoroughly researched and justified in [9, 8]. This has been generalized to limited data problems in the plane and to more general weights in [28].

Louis and Maaß have generalized Lambda CT to cone-beam CT [32] by replacing d^2/dp^2 by the Laplacian in the detector plane. Subsequently, Katsevich [27, 26], Anastasio *et al.* [1] and Ye *et al.* [51] have generalized this in ways analogous to what we do in SPECT. Quinto and Öktem [46] developed our methods for a related problem in electron microscopy.

3.3. Lambda CT for slant-hole SPECT. We now develop generalizations of Lambda CT to the slant-hole geometry. Recall for angle θ , the detector plane is the plane through the origin perpendicular to theta: θ^\perp . Let Δ_{θ^\perp} be the Laplacian in the detector plane θ^\perp . Our first method is to replace $-d^2/dy^2$ by $-\Delta_{\theta^\perp}$. Then we form

$$\mathcal{L}_\Delta f(x) = E_{-\nu}^* (- \Delta_{\theta^\perp} E_\nu f)(x) \quad (3.7)$$

Note that the calculation of $\mathcal{L}_\Delta f$ from data $E_\nu f$ is a local operation (for the same reasons as for Lambda CT), so the algorithm works for region of interest SPECT and for arbitrary curves on S^2 (see [46]).

To understand \mathcal{L}_Δ , we note that

$$\mathcal{L}_\Delta f(x) = -\Delta (E_{-\nu}^* E_\nu f) + \nu^2 E_{-\nu}^* E_\nu f \quad (3.8)$$

Now, (3.8) shows that \mathcal{L}_Δ has gives a sharpening term, $-\Delta(E_{-\nu}^* E_\nu f)$, plus a smoothing term, $\nu^2 E_{-\nu}^* E_\nu f$. The proof of (3.8) is given at the end of this section after appropriate coordinates are introduced.

The reconstructions in Figure 3 are better than in Figure 2, but why are there halos that seem to be below or above the out-of-plane disks? If

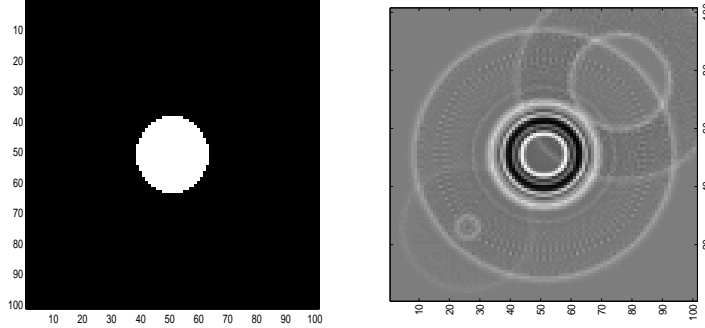


FIGURE 3. Cross-section with the $x - y$ plane of \mathcal{L}_Δ reconstruction of phantom given in Figure 2. The angle with the z -axis $\phi = \pi/4$.

we isolate the individual derivatives, we will see where they come from. We let $\theta : [0, 2\pi] \rightarrow C_\phi$ be the standard parameterization of C_ϕ :

$$\theta(a) = (\cos \phi \cos a, \cos \phi \sin a, \sin \phi).$$

Then the unit vector in the direction of the curve is $\alpha(a)$ and the vector perpendicular to $\theta(a)$ and $\alpha(a)$ is $\beta(a)$:

$$\alpha(a) = \frac{\theta'(a)}{\|\theta'(a)\|} = (-\sin a, \cos a, 0), \quad \beta(a) = \theta(a) \times \alpha(a) \quad (3.9)$$

This gives coordinates on $\theta^\perp(a)$

$$(r, s) \mapsto r\alpha(a) + s\beta(a) \quad (3.10)$$

and allows us to write the Laplacian on the detector plane

$$\Delta_{\theta^\perp} = \frac{d^2}{dr^2} + \frac{d^2}{ds^2}.$$

This gives two more operators

$$\mathcal{L}_r = E_{-\nu}^* \left(\frac{-d^2}{dr^2} E_\nu \right) f(x), \quad (3.11)$$

which takes a second derivative in the α direction, a direction tangent to the curve C_ϕ at $\theta(a)$ and

$$\mathcal{L}_s = E_{-\nu}^* \left(\frac{-d^2}{ds^2} E_\nu \right) f(x), \quad (3.12)$$

which takes a second derivative in the β direction, a direction perpendicular to the curve C_ϕ at $\theta(a)$.

Of course, $\mathcal{L}_\Delta = \mathcal{L}_r + \mathcal{L}_s$, but separating the derivatives shows the effects of each on the reconstructions in Figure 4. As one can see, \mathcal{L}_s adds singularities. If one looks closely at the \mathcal{L}_r reconstruction without smoothing, then one can see weaker singularities at the same places.

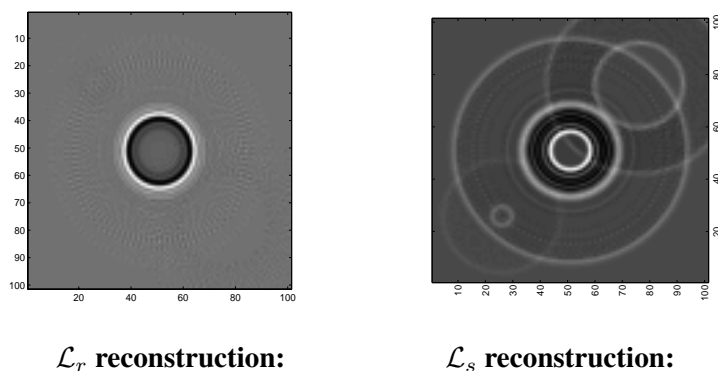


FIGURE 4. Cross-section with the $x - y$ plane of reconstructions of disks given in Figure 2. The angle with the z -axis $\phi = \pi/4$.

So, we see in the \mathcal{L}_s reconstruction in Figure 5, singularities are added. We can see them more clearly in the plane $x = y$, which is the plane containing the centers and the axis of rotation of the scanner.

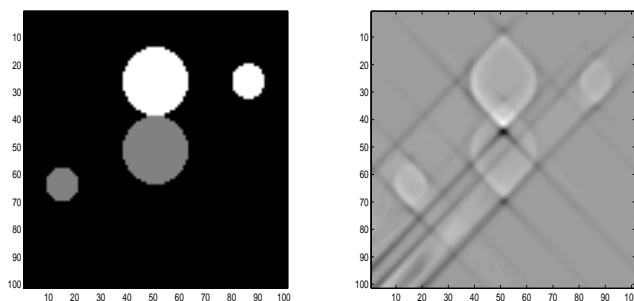


FIGURE 5. Phantom (left) and \mathcal{L}_s reconstruction (right) in the plane $x = y$ of disks given in Figure 2.

We point out that Ms. Bakhos has improved reconstructions that include noise and smoothing [3]. Furthermore, she and Ms. Chung have

added a factor $kE_{-\nu}^*E_\nu$ to provide the contour that Kennan Smith developed for standard planar lambda CT in [9] (see the discussion at the end of Section 3.2). Those reconstructions are better than the ones displayed here, but the singularities are not as visible, and the point of this article is to explore those singularities.

These reconstructions bring up two important questions. Why are some singularities (object boundaries) more clearly visible in our limited data reconstructions than others? Why are some singularities added to the \mathcal{L}_s and \mathcal{L}_r reconstructions? Why do the \mathcal{L}_s reconstructions seem to add stronger singularities? To answer these questions, we first need to establish what a singularity is, which we do in the next section.

PROOF OF (3.8). One starts with $\Delta E_{-\nu}^*E_\nu f$ and brings the Laplacian inside $E_{-\nu}^*E_\nu$ in expression (3.5). This shows that

$$\Delta E_{-\nu}^*E_\nu f(x) = \int_{a \in [0, 2\pi]} \int_{s \in \mathbb{R}} \Delta f(x + p\theta(a)) e^{\nu p} \sin \phi \, dp \, da \quad (3.13)$$

Now, inside the inner integral, one writes Δf in terms of the coordinates $(r, s, t) \mapsto r\alpha(a) + s\beta(a) + t\theta(a)$ for fixed $a \in [0, 2\pi]$. Thus, $\Delta f(x + p\theta(a))$ becomes

$$\left(\frac{\partial^2}{\partial r^2} + \frac{\partial^2}{\partial s^2} + \frac{\partial^2}{\partial t^2} \right) f(x + r\alpha(a) + s\beta(a) + (t + p)\theta(a)) \Big|_{(r,s,t)=\vec{0}}$$

Since the t derivative is evaluated at $t = 0$, we can replace the t derivative by the second derivative in p . Next, we separate the inner integral into two integrals, pull $\frac{\partial^2}{\partial r^2} + \frac{\partial^2}{\partial s^2}$ out of the first integral and do two integrations by parts in p (using the fact that f has compact support) in the second integral. The end result can be rearranged to get (3.8). \square

4. Singularities and wavefront sets

To understand what our operators do to singularities, we need to understand what singularities are. Practically they are density (absorption) jumps, boundaries between regions. Mathematically, they are where a function is not smooth, and we can characterize smoothness using the Fourier transform:

$$\begin{aligned} (\mathcal{F}f)(\xi) &= \tilde{f}(\xi) = \int_{x \in \mathbb{R}^n} e^{-ix \cdot \xi} f(x) dx, \\ f(x) &= \frac{1}{(2\pi)^n} \int_{\xi \in \mathbb{R}^n} e^{ix \cdot \xi} (\mathcal{F}f)(\xi) d\xi. \end{aligned} \quad (4.1)$$

The key idea is that rapid decrease at ∞ (faster than $1/\|\xi\|^m \forall m \in \mathbb{N}$) of $\mathcal{F}f$ is equivalent to smoothness of f . The following simple proposition makes this precise.

PROPOSITION 4.1. *Let f be a compactly supported integrable function. Then, $\mathcal{F}f$ is rapidly decreasing at ∞ (decreasing faster than any power of $1/\|x\|$) if and only if f is equal almost everywhere to a C^∞ function.*

PROOF. If $\mathcal{F}f$ is rapidly decreasing at ∞ , then one can take derivatives of all orders inside the integral in the inversion formula (4.1) and show that f is smooth. If f is smooth and of compact support, then $\mathcal{F}f$ is rapidly decreasing at ∞ as can be shown by proving the Fourier transforms of derivatives of f are bounded and are polynomials times $\mathcal{F}f$. \square

Sobolev spaces [41] are a natural generalization to L^2 integrability of this relationship between the Fourier transform and smoothness. A function smooth of Sobolev order $s \in \mathbb{N}$ has s derivatives in an L^2 sense.

DEFINITION 4.1. Let $s \in \mathbb{R}$ and let f be a distribution such that $\mathcal{F}f$ is a locally integrable function. Then $f \in H^s(\mathbb{R}^n)$ if

$$\|f\|_s = \left(\int_{\mathbb{R}^n} |\mathcal{F}f(\xi)|^2 (1 + \|\xi\|^2)^s d\xi \right)^{1/2}$$

is finite.

One can localize smoothness at a point x_0 by multiplying f by a smooth cut off function, $\varphi \in C_c^\infty(\mathbb{R}^n)$ with $\varphi(x_0) \neq 0$. If one does this, one develops the concept of Sobolev singular support.

DEFINITION 4.2. Let $s \in \mathbb{R}$ and $x_0 \in \mathbb{R}^n$, and let f be a distribution. Assume there is a cut off function that is nonzero near x_0 , $\varphi \in C_c^\infty(\mathbb{R}^n)$, such that the localized function φf is in $H^s(\mathbb{R}^n)$. Then we say f is *locally in H^s at x_0* . The H^s -singular support of f is the complement of the set of points at which f is locally in H^s .

The profound idea of Hörmander [25] and others is to microlocalize to characterize singularities more precisely. That is to find *directions* where $\mathcal{F}(\varphi f)$ is not rapidly decreasing at ∞ .

DEFINITION 4.3. Let $s \in \mathbb{R}$, $x_0 \in \mathbb{R}^n$ and $\xi_0 \in \mathbb{R}^n \setminus 0$. The function f is in H^s at x_0 in direction ξ_0 if there exists a cut-off function φ near x_0 and an open cone V with $\xi_0 \in V$ such that

$$\int_{\xi \in V} |\mathcal{F}(\varphi f)(\xi)|^2 (1 + \|\xi\|^2)^s d\xi \quad (4.2)$$

is finite

On the other hand, $(x_0, \xi_0) \in \text{WF}^s(f)$ if f is **not** in H^s at x_0 in direction ξ_0 .

The wavefront set can be defined for functions of (y, θ) using coordinates since WF^s is defined by cutoff functions.

EXAMPLE 4.4. If $f : \mathbb{R}^2 \rightarrow \mathbb{R}$ is equal to one on the right half plane and equal to zero on the left, then $\text{WF}^1(f)$ is the set of normals to the y -axis. One can prove this by calculating a localized Fourier transform of f at points on the y -axis. It can be shown [25] that one can use a special class of cut off functions that are products of functions in x with functions in y . This reduces the proof to doing integrations by parts in the x integral.

Moreover, the following generalization holds: if f has a jump singularity on a smooth closed surface S without boundary and is smooth elsewhere, then $\{(x, \xi) \mid x \in S, \xi \perp S \text{ at } x\} = \text{WF}^s(f)$ for s sufficiently large.

4.1. Singularity Detection in SPECT. In this section, we give the correspondence of singularities under E_ν . The key idea is that Radon transforms, such as E_ν , detect singularities perpendicular to the line (or plane or surface) being integrated over. However, some operators do not detect all perpendicular singularities, and in Definition 4.6 we describe the different types of singularities for E_ν . There are pure mathematical reasons for this [20, 22, 16, 46]. To clarify these singularities, before stating our main theorem, we define a geometric concept and then define three different types of singularities.

DEFINITION 4.5. Let C be a differentiable regular curve on the unit sphere parameterized by $\theta : (a_1, a_2) \rightarrow S^2$. Let $a \in (a_1, a_2)$ and $\theta_0 = \theta(a) \in C$. Let $\xi \in \mathbb{R}^3 \setminus 0$. We say ξ is *perpendicular to C at θ_0* if $\xi \cdot \theta'(a) = 0$.

DEFINITION 4.6. Let $L_0 = L(y_0, \theta_0)$ with $a \in [0, 2\pi]$, $\theta_0 = \theta(a) \in C_\phi$, $y_0 \in \theta_0^\perp$. Let $\xi \in \mathbb{R}^n \setminus 0$.

- (1) We say ξ is an *invisible* direction along L_0 if ξ is not perpendicular to L_0 . Equivalently, $\xi \notin \theta_0^\perp$.
- (2) We say ξ is a *bad* direction along L_0 if ξ is perpendicular to L_0 and perpendicular to C_ϕ at θ_0 . Equivalently, ξ is parallel $\beta(a)$.
- (3) We say ξ is a *good* direction along L_0 if ξ is perpendicular to L_0 but not perpendicular to C_ϕ at θ_0 . Equivalently, $\xi \in \theta_0^\perp$ and ξ is not parallel $\beta(a)$.

Note that the good, bad, and invisible directions in Definition 4.6 depend only on the direction, θ_0 , of the line L_0 .

THEOREM 4.7 (Microlocal Regularity of E_ν). *Let $L_0 = L(y_0, \theta_0)$ with $\theta_0 \in C_\phi$, $y_0 \in \theta_0^\perp$. Let f be a distribution of compact support.*

- i) If $E_\nu f$ is locally in H^s at (y_0, θ_0) , then f is in $H^{s-1/2}$ in directions η_0 at every point on L_0 for all **good** directions η_0 .*
- ii) If $E_\nu f$ is not locally in H^s at (y_0, θ_0) , then for some point $x \in L_0$ and some $\xi_0 \in \theta_0^\perp$, $(x, \xi) \in \text{WF}^{s-1/2}(f)$.*
- iii) Wavefront of f at invisible directions along L_0 does not affect the wavefront of $E_\nu f$ near L_0 .*

To summarize, this theorem implies that the exponential transform, E_ν , with limited data should detect a singularity of f when the line is perpendicular to the singularity (e.g., tangent to a boundary of part of the object) and the singularity is good. At bad directions, wavefront can be detected for some functions (as demonstrated by the streaks in our reconstructions starting from bad wavefront points), but not for others (see Example 4.11). If a singularity is invisible (not perpendicular to any line in the data set), then it will be harder to reconstruct stably. In Remark 4.13, we discuss what this all means for \mathcal{L}_Δ , \mathcal{L}_r , and \mathcal{L}_s .

Why does E_ν see singularities? Guillemin [19, 20] showed that Radon transforms are elliptic Fourier integral operators associated with a particular Lagrangian manifold (see also [42]). Then, Greenleaf and Uhlmann [16] developed the microlocal analysis of the X-ray transform on admissible complexes on manifolds. In the appendix we will use these ideas to prove a stronger version of Theorem 4.7 that gives the exact microlocal correspondence for good singularities and is true for E_ν , R_μ and any transform on the more general complex Y_C (3.2) and any smooth nowhere zero weight (see (A.4)). Similarly, our reconstruction methods are valid for any curve C on S^2 [46] and any smooth measures.

4.2. Examples and Observations. We will now go through a series of examples that illustrate the different types of singularities and how E_ν detects them. Our next example shows heuristically how E_ν can detect singularities perpendicular to the line being integrated over but not others.

EXAMPLE 4.8. Let f be equal to one inside the unit disk, B and zero outside. Let S be the boundary of B . Then, the only wavefront of f is at points on the S in directions normal S . In other words, $\text{WF}(f)$ is the set of (x, ξ) with $x \in S$, ξ perpendicular to S at x [25]. Let $(y_0, \theta_0) \in Y_\phi$ and assume the line $L_0 = L(y_0, \theta_0)$ is tangent to S at the point x_0 . Let ξ_0 be normal to S at x_0 . Then, we know $(x_0, \xi_0) \in \text{WF}(f)$ and f is smooth

at all other points $x \neq x_0$ on L_0 . Note that ξ_0 is normal to L_0 , because L_0 is tangent to S at x_0 . Also, the function

$$\theta_0^\perp \ni y \mapsto E_\nu f(y, \theta_0)$$

is not smooth at y_0 since $E_\nu f(\cdot, \theta_0)$ becomes nonzero in a non-smooth way as y and $L(y, \theta_0)$ move into B . Thus, in this simple case, this singularity perpendicular to L_0 is detected by the data $E_\nu f$. Note that if $L(y, \theta_0)$ meets the interior of the disk, then $E_\nu f(y, \theta_0)$ is smooth until the line becomes tangent again to the boundary of the disk. When the line $L(y, \theta_0)$ meets the interior of B , then f has no singularities perpendicular to the line (the singularities of f along the line are at boundary points and the directions are not perpendicular to the line). This illustrates iii) of Theorem 4.7.

Example 4.8 shows heuristically that E_ν detects only singularities perpendicular to the line being integrated over. However, E_ν does unpredictable things to bad singularities. We will now describe the bad directions geometrically.

EXAMPLE 4.9. Let $\theta_0 = \theta(a) \in C_\phi$ and $y_0 \in \theta_0^\perp$. Now let $L_0 = L(y_0, \theta_0)$.

Here is one way to describe the bad directions geometrically. Recall that \mathfrak{C}_ϕ is the cone through the origin with opening angle ϕ with the z -axis. Let $x \in L_0$. Consider the cone $x + \mathfrak{C}_\phi$. Then, L_0 is a line on this cone and there is a plane P_x that is tangent to $x + \mathfrak{C}_\phi$ and contains L_0 . The vector ξ is perpendicular to this tangent plane iff it is bad. To see this, first assume ξ is perpendicular to P_x . Then, ξ is perpendicular to L_0 since $L_0 \subset P_x$, and furthermore, ξ must be perpendicular to C_ϕ at θ_0 because ξ is perpendicular to $x + \mathfrak{C}_\phi$ along L_0 and therefore perpendicular to \mathfrak{C}_ϕ along the line $L(0, \theta_0)$. That means that ξ is perpendicular to the circle $C_\phi \subset \mathfrak{C}_\phi$ at θ_0 . Reverse these arguments to prove the other direction.

It should be pointed out that the condition that P_x is the same plane for each $x \in L_0$ is part of the definition of admissible line complex [13, 14, 15, 20].

A second way to describe bad directions is as directions that are parallel $\beta(a)$ (see (3.9)).

Finally, the direction ξ is bad along L_0 iff it is perpendicular to $\theta(a)$ and in the plane containing $\theta(a)$ and the z -axis. Here is why. By shifting the argument above to $x = 0$, ξ is bad along L_0 iff ξ perpendicular the plane P_0 that contains $L(0, \theta_0)$ and is tangent to the cone \mathfrak{C}_ϕ . Since P_0 is tangent to \mathfrak{C}_ϕ , to be perpendicular to P_0 is equivalent to being perpendicular to θ_0 and in the plane containing θ_0 and the z -axis (the axis of the cone \mathfrak{C}_ϕ).

REMARK 4.10. We can learn from some useful observations of Orlov for the parallel beam transform $P = E_0$ with directions on a curve C . Let $\theta \in C$ and let \mathcal{F}_y be the Fourier transform on the plane θ^\perp , $\mathcal{F}_y g(\sigma, \theta) = \int_{y \in \theta^\perp} g(y, \theta) e^{-iy \cdot \sigma} dy$ for $\sigma \in \theta^\perp$. Then the well-known Projection Slice Theorem [38] for $\theta \in S^2$ and for $\sigma \in \theta^\perp$ is

$$\mathcal{F}f(\sigma) = \mathcal{F}_y(Pf(\sigma, \theta)) \quad (4.3)$$

Therefore, if data $Pf(y, \theta)$ is given for $(y, \theta) \in Y_C = \{(y, \theta) \mid \theta \in C, y \in \theta^\perp\}$ (see (3.2)), then the Fourier transform $\mathcal{F}f(\sigma)$ is known on the *dual cone* to C , the cone

$$\bigcup_{\theta \in C} \theta^\perp. \quad (4.4)$$

For Y_ϕ , this dual cone is exactly the cone generated by the spherical band in Figure 6 (the vectors in a sphere centered at the origin are normal to the sphere). In fact, these are exactly the directions in which the wavefront of f is visible plus the bad directions by Theorem 4.7. Note that $\mathcal{F}f$ known from this data only at directions in the dual cone. Using (4.3), Orlov [40] developed an inversion method for P as long as all Fourier directions are recovered from integrals over lines in the complex Y_C . Orlov's condition for invertibility is that $\mathbb{R}^3 = \cup_{\theta \in C} \theta^\perp$. Under Orlov's condition, $\mathcal{F}f$ is known on all of \mathbb{R}^3 , so f can be recovered by Fourier inversion.

EXAMPLE 4.11. In our reconstructions, you have seen how singularities of f in the bad directions can be spread. In this example, we show the opposite, namely how wavefront in the bad directions can be undetected. It is easiest to do this for $P = E_0$ because of the Projection Slice Theorem (4.3). Let $\phi \in (0, \pi/2)$. Let ξ_0 be a bad direction. We construct a function f with $Pf \equiv 0$ on Y_ϕ (so Pf is smooth on Y_ϕ) but f has wavefront in this bad direction. This example also shows that P restricted to data on Y_ϕ is not injective for functions not of compact support.

First we describe the Fourier transform, $\mathcal{F}f$. Let \mathcal{C}_P be the solid cone about the ξ_3 -axis with opening angle $\pi/2 - \phi$. Note that \mathcal{C}_P is the complement of the dual cone to C_ϕ (see (4.4)). To define $\mathcal{F}f$, first take a homogeneous function of sufficiently negative degree that is supported in a conic neighborhood of ξ_0 , nonzero at ξ_0 , and smooth away from the origin. Then, alter the function near 0 to make it zero near the origin and smooth on \mathbb{R}^3 . Finally, make it zero off of \mathcal{C}_P . Call the result \hat{h} . Next, (to make f integrable) we define

$$\mathcal{F}(f)(\xi) = \hat{h}(\xi) \left(\frac{\xi}{\|\xi\|} \cdot (0, 0, 1) - \cos \phi \right)^k$$

for sufficiently large $k \in \mathbb{N}$. By construction, $\mathcal{F}f$ is rapidly decreasing in no neighborhood of ξ_0 . Therefore, ξ_0 is not in the limit cone at infinity of $\text{supp } \mathcal{F}f$, and so, by [25, Lemma 8.1.7, p. 258], for any point $x \in \mathbb{R}^3$, $(x, \xi_0) \in \text{WF}(f)$. Therefore $(x, \xi) \in \text{WF}^s(f)$ for sufficiently large s .

Because $\mathcal{F}f$ is homogeneous of high negative degree at infinity and goes to zero like $(\frac{\xi}{\|\xi\|} \cdot (0, 0, 1) - \cos \phi)^k$ near $\text{bd}(\mathcal{C}_P)$ if k is large enough, $\mathcal{F}f$ is sufficiently smooth and integrable for f to be integrable.

Finally, because $\mathcal{F}f$ is zero on the dual cone to C_ϕ , by the Projection Slice Theorem argument in the last example, $Pf \equiv 0$ on Y_ϕ . For any bad direction, we have constructed a nonzero function f that is integrable, $Pf \equiv 0$ and $(x, \xi_0) \in \text{WF}(f)$ for all $x \in \mathbb{R}^3$.

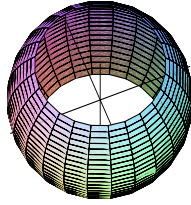


FIGURE 6. This figure, illustrating Example 4.12, shows the points on the unit sphere $S = \text{bd}(B)$ corresponding to good, bad, and invisible wavefront directions when $\phi = \pi/4$. The z -axis, the axis of rotation of the equatorial band, is the axis coming up out of the sphere. The open equatorial band represents points on the sphere with singularities in good directions. The latitude circles at the boundary of the band represent points with singularities in the bad directions. The top and bottom spherical caps correspond to points with invisible singularities.

EXAMPLE 4.12. In Figure 6, we show the good, bad, and invisible singularities for a special case related to the phantom in our reconstructions. If f is the characteristic function of the unit disk, B , then $\text{WF}(f)$ is the set of normals to $S := \text{bd}(D)$, and Figure 6 shows points on the boundary with good, bad, and invisible singularities. Since S is the unit sphere, each point on S is also normal to S . The invisible singularities correspond to points on S not normal to any line in Y_ϕ , and these are exactly the spherical caps at the north and south pole.

By Definition 4.6, good and bad singularities are in the dual cone to the circle C_ϕ (see (4.4) and Theorem 4.7):

$$\mathcal{D}_\phi = \bigcup_{\theta \in C_\phi} \theta^\perp$$

and by the correspondence between normal directions and points on S , points corresponding to good and bad singularities are on $S \cap \mathcal{D}_\phi$, that is all points with angle from the z -axis greater than or equal to $\pi/2 - \phi$.

We now explain why the bad singularities are at points on the boundary of this spherical band. Let x_0 be a point on S corresponding to a bad direction. Since x_0 is normal to S at x_0 , x_0 must be a bad direction itself. Since bad directions correspond to singularities in planes containing $\theta \in C_\phi$ and the z -axis (see Definition 4.6 (2) and the discussion at the end of Example 4.9), the angle between x_0 and the z -axis is $\pi/2 - \phi$. Thus, x_0 is at the boundary of the spherical band.

Let $L_0 = L(y_0, \theta_0)$ be the line in the complex Y_ϕ tangent to S at x_0 . Because θ_0 and x_0 are in the same plane as the z -axis, L_0 must be in that plane and so L_0 intersects the z -axis. Furthermore, using geometry, one sees that the union of the lines for all points x_0 on the top (or bottom) boundary of the band form a cone with center on the z -axis and opening angle ϕ , that is a cone parallel \mathfrak{C}_ϕ and tangent to S along a circle.

\mathcal{L}_Δ , \mathcal{L}_r , or \mathcal{L}_s can spread singularities of f that are in bad directions. We can see this from the reconstructions in Figures 3, 4, 5. Now that we have a geometric way of understanding bad directions, we see the singularities are spread along lines in the data set that are perpendicular to bad directions. In the case of this characteristic function f , we have shown that those lines form the two cones that are parallel \mathfrak{C}_ϕ and tangent to S . Looking at the reconstructions in Figures 2, 3, 4, 5 we see that the singularities are spread along these cones that are tangent to each sphere, and they cause the halo circles or lines in those reconstructions.

REMARK 4.13. The microlocal reason why \mathcal{L}_r and \mathcal{L}_s add singularities is beyond this article and we plan to prove this in a subsequent article. The general phenomenon is discussed in [16] and for cone beam tomography (a related but different transform from ours) in [12, 27, 26]. The reasons, as we will prove in a subsequent article, are that \mathcal{L}_Δ , \mathcal{L}_r and \mathcal{L}_s are pseudodifferential operators that are singular in the bad directions. The reconstructions (and examples in [46]) show how singularities in the bad directions can be smeared. \mathcal{L}_r doesn't take derivatives in the bad directions (the $\beta(a)$ direction, perpendicular to C at θ), and reconstructions don't accentuate the added singularities in this bad direction.

Because \mathcal{L}_s takes derivatives in the bad directions, the added singularities are stronger (less differentiable in Sobolev scale). Note that the idea behind \mathcal{L}_r —taking a derivative in a good direction in the detector plane—is the reason the improved cone beam algorithms of [1, 26, 51] work well.

REMARK 4.14. Wavefront singularities are defined by slow decay at ∞ of $\mathcal{F}f$. But, one can argue that slow decay is not measurable from numerical data. However, for the standard discontinuities of tomographic data, this slow decay occurs sufficiently close to zero to be numerically visible. This has not been quantified, but Rullgård and Quinto are working on local band-limited Sobolev seminorms to do this.

E_ν is injective for functions of compact support because, of course, there are inversion formulas. But, the restricted region of interest transform is not injective. For $\nu = 0$, this can be seen by a modification of a two-dimensional counterexample to injectivity for the interior problem [3].

Null functions for region of interest slant-hole SPECT, the ones that cause problems for reconstruction algorithms, are oscillatory (large high Fourier coefficients), and good reconstruction methods filter them out. Also, singularity detection methods like Lambda CT and our methods recover singularities of an object, and this is a sort of regularization. We don't try to recover the values of the data, but only the singularities that are stably visible from the data according to Theorem 4.7 (in good directions).

Appendix A. Microlocal properties of E_ν and the generalized transform \mathcal{P}_m

We consider general X-ray transforms over arbitrary curves. Let $a_1 < a_2$ and consider the curve C that is parameterized by the smooth regular function $\theta : (a_1, a_2) \rightarrow S^2$. We can assume that the parameterization θ is chosen so $\|\theta'\| \equiv 1$ without loss of generality.

We use the following notation

$$\alpha(a) = \theta'(a), \quad \beta(a) = \theta(a) \times \alpha(a) \quad (\text{A.1})$$

Note that $\alpha(a)$, $\beta(a)$, $\theta(a)$ form an orthonormal basis of \mathbb{R}^3 and $\alpha(a)$ and $\beta(a)$ form an orthonormal basis of $\theta^\perp(a)$.

We assume the following *curvature condition*

$$\forall a \in (a_1, a_2), \quad \theta''(a) \cdot \theta(a) \neq 0. \quad (\text{A.2})$$

This is easily seen to be true for the slant-hole geometry.

We use coordinates on Y_C (3.2) to make the calculation easier

$$\begin{aligned} \mathcal{Y}_C &= \mathbb{R}^2 \times (a_1, a_2) \ni (r, s, a) \mapsto (r\alpha(a) + s\beta(a), \theta(a)) \in Y_C \\ \mathcal{L}(r, s, a) &= L(r\alpha(a) + s\beta(a), \theta(a)) \end{aligned} \quad (\text{A.3})$$

and we consider the parallel beam transform on \mathcal{Y}_C with arbitrary C^∞ weight that is nowhere zero

$$\mathcal{P}_m(f)(r, s, a) = \int_{x \in \mathcal{L}(r, s, a)} f(x) m(x, (r, s, a)) dx_L. \quad (\text{A.4})$$

Of course, both E_ν and R_μ fit into this framework with $Y_C = Y_\phi$ as long as, for R_μ , the attenuation μ is smooth.

Wavefront sets are defined on cotangent spaces, and we will observe this convention now so that readers who compare our results to the classical ones can easily see the relation. We need to change some notation. Instead of using tangent vectors, we use the dual cotangent vectors. Let $x = (x_1, x_2, x_3) \in \mathbb{R}^3$. Associated to the tangent vector $\xi_1 \frac{\partial}{\partial x_1} + \xi_2 \frac{\partial}{\partial x_2} + \xi_3 \frac{\partial}{\partial x_3}$ is its dual cotangent vector,

$$\begin{aligned} (x; \xi \mathbf{dx}) \text{ where } \xi &:= (\xi_1, \xi_2, \xi_3) \text{ and} \\ \xi \mathbf{dx} &:= \xi_1 \mathbf{dx}_1 + \xi_2 \mathbf{dx}_2 + \xi_3 \mathbf{dx}_3. \end{aligned}$$

We make a similar convention for $T^*(\mathcal{Y}_C)$, namely, the covector above (r, s, a) on \mathcal{Y}_C is denoted

$$((r, s, a); \eta_r \mathbf{dr} + \eta_s \mathbf{ds} + \eta_a \mathbf{da}). \quad (\text{A.5})$$

THEOREM A.1. *Let f be a distribution of compact support on \mathbb{R}^3 . Assume $\mathcal{P}_m(f)$ is given on an open set $U \subset \mathcal{Y}_C$. Let $(r, s, a) \in U$ and let ξ be a non-zero vector perpendicular to $\theta(a)$ written as*

$$\xi = \xi_r \alpha(a) + \xi_s \beta(a).$$

Finally, let $x \in \mathcal{L}(r, s, a)$. If $\xi_r \neq 0$ (i.e., ξ is not parallel $\beta(a)$), then

$$\begin{aligned} (x; \xi \mathbf{dx}) &\in \text{WF}^\alpha(f) \text{ if and only if} \\ \left((r, s, a); \xi_r \mathbf{dr} + \xi_s \mathbf{ds} + x \cdot (\xi_r \theta''(a) + \xi_s \theta(a) \times \theta''(a)) \mathbf{da} \right) & \quad (\text{A.6}) \\ &\in \text{WF}^{\alpha+1/2}(\mathcal{P}_m(f)). \end{aligned}$$

Note that the condition $\xi_r \neq 0$ is equivalent to ξ being a good direction (one that is not parallel $\beta(a)$).

PROOF. The proof follows from more general results in [16] (see also [5]). We provide a proof for completeness. First, we calculate the canonical relation [24] of \mathcal{P}_m , which is given in the following lemma.

LEMMA A.2. \mathcal{P}_m is an elliptic Fourier integral operator (FIO) of order $-1/2$ with canonical relation

$$\begin{aligned} \mathcal{C} = \left\{ \left(x, (r, s, a); (\eta_r \alpha(a) + \eta_s \beta(a)) \mathbf{d}\mathbf{x}, \right. \right. \\ \left. \left. \eta_r \mathbf{d}\mathbf{r} + \eta_s \mathbf{d}\mathbf{s} + x \cdot (\eta_r \theta''(a) + \eta_s (\theta(a) \times \theta''(a))) \mathbf{d}\mathbf{a} \right) \right. \\ \left. \left| (\eta_r, \eta_s) \neq \mathbf{0}, x \cdot \alpha(a) - r = 0, x \cdot \beta(a) - s = 0 \right. \right\}. \end{aligned} \quad (\text{A.7})$$

PROOF. The *incidence relation* of a Radon transform is defined to be the set of ordered pairs of points x and manifolds of integration $L \in Y$ such that $x \in L$. So, the incidence relation of \mathcal{P}_m [23, 15] can be written in our coordinates

$$Z := \{ (x, (r, s, a)) \mid x \cdot \alpha(a) - r = 0, x \cdot \beta(a) - s = 0 \} \quad (\text{A.8})$$

since $x \in \mathcal{L}(r, s, a)$ if and only if the equations given in (A.8) hold. Then, the following properties were shown in general for Radon transforms [19, 21, 42] and, as we will explain, apply to \mathcal{P}_m . First, the Schwartz kernel of any Radon transform is integration over its incidence relation, Z [42, Proposition 1.1]. Thus, the Schwartz kernel is a conormal distribution associated with Lagrangian manifold the conormal bundle of Z , $N^*(Z) \setminus 0$, [19, 42]. Furthermore, under assumptions we will establish for \mathcal{P}_m , the Radon transform is an elliptic Fourier Integral Operator (FIO) that is associated with the Lagrangian manifold $N^*Z \setminus \{0\}$. To show this for \mathcal{P}_m , we need to calculate $N^*Z \setminus \{0\}$ for this transform. Z is defined, (A.8), by equations $x \cdot \alpha(a) - r = 0$, $x \cdot \beta(a) - s = 0$, and so above each $(x, (r, s, a)) \in Z$, N^*Z has as basis

$$\alpha(a) \mathbf{d}\mathbf{x} - \mathbf{d}\mathbf{r} - x \cdot \alpha'(a) \mathbf{d}\mathbf{a}, \quad \beta(a) \mathbf{d}\mathbf{x} - \mathbf{d}\mathbf{s} - x \cdot \beta'(a) \mathbf{d}\mathbf{a}, \quad (\text{A.9})$$

and any covector above $(x, (r, s, a))$ is a linear combination of these covectors. Since $\alpha'(a) = \theta''(a)$ and $\beta'(a) = \theta(a) \times \theta''(a)$ we see that

$$\begin{aligned} N^*Z \setminus \{0\} = \left\{ \left(x, (r, s, a); (\eta_r \alpha(a) + \eta_s \beta(a)) \mathbf{d}\mathbf{x}, \right. \right. \\ \left. \left. -\eta_r \mathbf{d}\mathbf{r} - \eta_s \mathbf{d}\mathbf{s} - x \cdot (\eta_r \theta''(a) + \eta_s \theta(a) \times \theta''(a)) \mathbf{d}\mathbf{a} \right) \right. \\ \left. \left| (\eta_r, \eta_s) \neq \mathbf{0}, x \cdot \alpha(a) - r = 0, x \cdot \beta(a) - s = 0 \right. \right\}. \end{aligned} \quad (\text{A.10})$$

The canonical relation of an operator is gotten from its Lagrangian manifold by multiplying the last coordinates (the cotangent coordinates in

\mathbf{dr} , \mathbf{ds} , and \mathbf{da} , those above Y_C) by -1 . This concludes the proof of Lemma A.2. \square

The proof of (A.6) follows from Lemma A.2. Let $p_Y : \mathcal{C} \rightarrow T^*(\mathcal{Y}_C)$ be the projection on the second coordinates,

$$\begin{aligned} p_Y & \left(x, (r, s, a); (\eta_r \alpha(a) + \eta_s \beta(a)) \mathbf{dx}, \right. \\ & \left. \eta_r \mathbf{dr} + \eta_s \mathbf{ds} + x \cdot (\eta_r \theta''(a) + \eta_s \theta(a) \times \theta''(a)) \mathbf{da} \right) \\ & := \left((r, s, a); \eta_r \mathbf{dr} + \eta_s \mathbf{ds} + x \cdot (\eta_r \theta''(a) + \eta_s \theta(a) \times \theta''(a)) \mathbf{da} \right) \end{aligned} \quad (\text{A.11})$$

and let $p_X : \mathcal{C} \rightarrow T^*(\mathbb{R}^3)$ be the projection

$$\begin{aligned} p_X & \left(x, (r, s, a); (\eta_r \alpha(a) + \eta_s \beta(a)) \mathbf{dx}, \right. \\ & \left. \eta_r \mathbf{dr} + \eta_s \mathbf{ds} + x \cdot (\eta_r \theta''(a) + \eta_s \theta(a) \times \theta''(a)) \mathbf{da} \right) \\ & := (x; (\eta_r \alpha(a) + \eta_s \beta(a)) \mathbf{dx}). \end{aligned} \quad (\text{A.12})$$

We need to check that p_Y maps \mathcal{C} to $T^*(\mathcal{Y}_C) \setminus \{0\}$. This is clear from (A.11) since $(\eta_r, \eta_s) \neq (0, 0)$. Similarly the projection p_X to $T^*(\mathbb{R}^3)$ maps to $T^*(\mathbb{R}^3) \setminus \{0\}$. These conditions show that \mathcal{P}_m is a FIO [24]. \mathcal{P}_m is elliptic because its symbol is smooth, nowhere zero, and constant in the cotangent variable (see [42, (14), (15)]). Because the codimension of Z in $\mathbb{R}^3 \times \mathcal{Y}_C$ is two, \mathcal{P}_m has order $-1/2$ [21, 16].

Define

$$\begin{aligned} \mathcal{N} = \left\{ (x, (r, s, a); \eta_s \beta(a) \mathbf{dx}, \eta_s (\mathbf{ds} + x \cdot (\theta(a) \times \theta''(a)) \mathbf{da}) \right. \\ \left. \mid x \in \mathcal{L}(r, s, a), \eta_s \neq 0 \right\}, \end{aligned} \quad (\text{A.13})$$

and note that \mathcal{N} is just the set of points in \mathcal{C} for which $\eta_r = 0$. The set \mathcal{N} corresponds to the bad directions.

We finally need to check that $p_Y : (\mathcal{C} \setminus \mathcal{N}) \rightarrow T^*(\mathcal{Y}_C)$ is an injective immersion. This is a microlocal Bolker assumption [21] [42, (9)]. Under this assumption, one can compose \mathcal{P}_m and a dual transform microlocalized to be zero near \mathcal{N} and use the calculus of microlocally elliptic pseudodifferential and Fourier integral operators to show (A.6) (e.g., [21, 42]). Here is the proof of the microlocal Bolker assumption. From the image in (A.11), we know r, s, a, η_r, η_s as well as

$$\begin{aligned} x_{\theta^\perp} & := r\alpha(a) + s\beta(a), \quad \xi \mathbf{dx} = (\eta_r \alpha(a) + \eta_s \beta(a)) \mathbf{dx}, \\ A & := \eta_r x \cdot \theta''(a) + \eta_s x \cdot (\theta(a) \times \theta''(a)). \end{aligned} \quad (\text{A.14})$$

Note that A is the coefficient of $\mathbf{d}a$ in the image in (A.11). Since x_{θ^\perp} is the projection of x to the plane θ^\perp ,

$$x \cdot (\theta(a) \times \theta''(a)) = x_{\theta^\perp} \cdot (\theta(a) \times \theta''(a)).$$

So, the only information we need in order to find $(x, \xi \mathbf{d}x)$ and prove p_Y is an injective immersion when $\eta_r \neq 0$ is to find t in the expression

$$x = t\theta(a) + x_{\theta^\perp}. \quad (\text{A.15})$$

By plugging (A.15) into the formula for A in (A.14), one can easily show that

$$t = \frac{A - x_{\theta^\perp} \cdot (\eta_r \theta''(a) + \eta_s \theta(a) \times \theta''(a))}{\eta_r \theta(a) \cdot \theta''(a)} \quad (\text{A.16})$$

and so t is smoothly determined, and p_Y is an injective immersion off of \mathcal{N} . Note that here we are using the curvature condition (A.2) and our assumption that we are off of \mathcal{N} ($\eta_r \neq 0$) to know that the denominator in (A.16) is not zero. Then, in exactly the same way as in [42], for example, this shows that the Bolker Assumption holds off of \mathcal{N} .

The map p_X is an immersion off of \mathcal{N} because p_Y is an immersion and $N^*(Z) \setminus \{0\}$ is Lagrangian [24]. If the curve C does not include antipodal points (if $\theta \in C$ then $-\theta \notin C$), then that p_X is injective off of \mathcal{N} . This can be seen because, as long as $\eta_a \neq 0$, the plane ξ^\perp intersects C transversely. In case the curve of directions C includes a point θ and its antipodal point, $-\theta$, one can just localize C around θ and use the microlocal analysis we will now give for this localized curve. In either case, this argument and standard microlocal analysis [24] shows that as long as $\eta_r \neq 0$ (off of \mathcal{N}),

$$(x, \xi) \in \text{WF}(f) \text{ iff } p_Y \circ (p_X)^{-1}(x, \xi \mathbf{d}x) \in \text{WF}(\mathcal{P}_m(f)). \quad (\text{A.17})$$

When one traces (A.17) back, one gets exactly (A.6) for smooth wavefront set. To get (A.6) for Sobolev wavefront set, one needs to use that \mathcal{P}_m is an elliptic FIO of order $-1/2$ associated to a local canonical graph off of \mathcal{N} , and Sobolev continuity of order $-1/2$ holds for such operators (when localized away from \mathcal{N}). This is very similar to the arguments in [44, 46, 45] for Sobolev and real-analytic wavefront set. This concludes the proof of Theorem A.1. \square

It should be pointed out that \mathcal{N} in (A.13) is the set on which p_Y is not an injective immersion and it causes singularities of $f \in \mathcal{E}'(\mathbb{R}^3)$ to be moved if one forms $\mathcal{P}_m^* \mathcal{P}_m f$, as shown in [16]. This is also observed for other tomographic transforms including the ones for cone beam CT [16, 27, 12] and for electron microscopy [46].

References

1. Mark A. Anastasio, Yu Zou, Emil Y. Sudley, and Xiaocuan Pan, *Local cone-beam tomography image reconstruction on chords*, Journal of the Optical Society of America A **24** (2007), 1569–1579.
2. E.V. Arbutov, A.L. Bukhgeim, and S.G. Kasantzev, *Two-dimensional tomography problems and the theory of A -analytic functions*, Siberian Adv. in Math. **8** (1998), no. 4, 1–20.
3. Tania Bakhos, *Local Algorithms in Slant-Hole Spect*, Tech. report, Tufts University, 2008, Senior Honors Thesis.
4. Jan Boman, *An Example of Non-uniqueness for a generalized Radon transform*, J. d'Analyse Mathématique (1993), 395–401.
5. Jan Boman and Eric Todd Quinto, *Support theorems for real analytic Radon transforms on line complexes in \mathbb{R}^3* , Trans. Amer. Math. Soc. **335** (1993), 877–890.
6. Sohhyun Chung, *Reconstruction Algorithms in Slant-hole Single Photon Emission Computed Tomography(SPECT)*, Tech. report, Tufts University, 2006, Senior Honors Thesis.
7. E. Derevtsov, R. Dietz, T. Schuster, and A.K. Louis, *Influence of refraction to the accuracy of a solution for the 2D-emission tomography problem*, J. Inv. Ill-Posed Prob. **8** (2000), 161–191.
8. Adel Faridani, David Finch, E. L. Ritman, and Kennan T. Smith, *Local tomography, II*, SIAM J. Appl. Math. **57** (1997), 1095–1127.
9. Adel Faridani, E. L. Ritman, and Kennan T. Smith, *Local tomography*, SIAM J. Appl. Math. **52** (1992), 459–484.
10. David V. Finch, *The attenuated X-ray transform: recent developments*, Inside - Out: Inverse Problems and applications (Cambridge, UK) (G. Uhlmann, ed.), Cambridge University Press, 2004.
11. David Victor Finch, *Uniqueness for the attenuated X-ray transform in the physical range*, SIAM J. Appl. Math. (1986), 197–203.
12. David Victor Finch, Ih-Ren Lan, and Gunther Uhlmann, *Microlocal Analysis of the Restricted X-ray Transform with Sources on a Curve*, Inside Out, Inverse Problems and Applications (Gunther Uhlmann, ed.), MSRI Publications, vol. 47, Cambridge University Press, 2003, pp. 193–218.
13. Israel M. Gelfand and M. I. Graev, *Integral transformations connected with straight line complexes in a complex affine space*, Soviet Math. Doklady **2** (1961), 809–812.
14. Israel M. Gelfand, M. I. Graev, and Radu Rosu, *The problem of integral geometry for p -dimensional planes in real projective spaces (the non-local variant)*, Operator Algebras and Group Representations, vol. I, Pitman, Inc., 1982, pp. 192–207.
15. Israel M. Gelfand, M. I. Graev, and Z. Ya. Shapiro, *Differential forms and integral geometry*, Functional Anal. and Appl. **3** (1969), 24–40.
16. Allan Greenleaf and Gunther Uhlmann, *Non-local inversion formulas for the X-ray transform*, Duke Math. J. **58** (1989), 205–240.
17. ———, *Microlocal techniques in integral geometry*, Contemporary Math. **113** (1990), 121–136.
18. J.-P. Guillemin, F. Jauberteau, L. Kunyansky, R. Novikov, and R. L. Trebassen, *On single-photon emission computed tomography imaging based on an exact formula for the nonuniform attenuation correction*, Inverse Problems **18** (2002), L11–L19.
19. Victor Guillemin, *Some remarks on integral geometry*, Tech. report, MIT, 1975.

20. ———, *On some results of Gelfand in integral geometry*, Proceedings Symposia Pure Math. **43** (1985), 149–155.
21. Victor Guillemin and Shlomo Sternberg, *Geometric Asymptotics*, American Mathematical Society, Providence, RI, 1977.
22. ———, *Some problems in integral geometry and some related problems in micro-local analysis*, Amer. J. Math. **101** (1979), 915–955.
23. Sigurdur Helgason, *The surjectivity of invariant differential operators on symmetric spaces I*, Annals Math. **98** (1973), 451–479.
24. Lars Hörmander, *Fourier Integral Operators, I*, Acta Mathematica **127** (1971), 79–183.
25. ———, *The Analysis of Linear Partial Differential Operators*, vol. I, Springer Verlag, New York, 1983.
26. Alexander Katsevich, *Improved Cone Beam Local Tomography*, Inverse Problems **22** (2006), 627–643.
27. Alexander I. Katsevich, *Cone beam local tomography*, SIAM J. Appl. Math. **59** (1999), 2224–2246.
28. Peter Kuchment, Kirk Lancaster, and Ludmilla Mogilevskaya, *On local tomography*, Inverse Problems **11** (1995), 571–589.
29. Peter Kuchment and Eric Todd Quinto, *Some problems of integral geometry arising in tomography*, The Universality of the Radon Transform, by Leon Ehrenpreis, Oxford University Press, London, 2003.
30. L. Kunyansky, *A new SPECT reconstruction algorithm based on the Novikov’s explicit inversion formula*, Inverse Problems **17** (2001), 293–306.
31. ———, *Inversion of the 3-D exponential parallel-beam transform and Radon transform with angle-dependent attenuation*, Inverse Problems **20** (2004), 1455–1478.
32. Alfred K. Louis and Peter Maaß, *Contour reconstruction in 3-D X-Ray CT*, IEEE Trans. Medical Imaging **12** (1993), no. 4, 764–769.
33. Andrew Markoe, *Fourier inversion of the attenuated X-ray transform*, SIAM J. Math. Anal. **15** (1984), 718–722.
34. R. G. Mukhometov, *The problem of recovery of a 2-dimensional Riemannian metric and integral geometry*, Soviet Math. Dokl. **18** (1977), 27–31.
35. Frank Natterer, *Computerized tomography with unknown sources*, SIAM J. Appl. Math. **43** (1983), 1201–1212.
36. ———, *Inversion of the attenuated Radon transform*, Inverse Problems **17** (2001), 113–119.
37. ———, *The mathematics of computerized tomography*, Classics in Mathematics, Society for Industrial and Applied Mathematics, New York, 2001.
38. Frank Natterer and Frank Wübbeling, *Mathematical Methods in image Reconstruction*, Monographs on Mathematical Modeling and Computation, Society for Industrial and Applied Mathematics, New York, 2001.
39. R. Novikov, *Une formule d’inversion pour la transformation d’un rayonnement X atténué*, C. R. Acad. Sci. Paris Ser. I Math **332** (2001), no. 12, 1059–1063.
40. S.Š. Orlov, *Theory of three dimensional reconstruction. I. Conditions of a complete set of projections*, Sov. Phys.-Crystallogr. **20** (1975), 312–314.
41. Bent Petersen, *Introduction to the Fourier Transform and Pseudo-Differential Operators*, Pittman, Boston, 1983.
42. Eric Todd Quinto, *The dependence of the generalized Radon transform on defining measures*, Trans. Amer. Math. Soc. **257** (1980), 331–346.

43. ———, *The invertibility of rotation invariant Radon transforms*, J. Math. Anal. Appl. **94** (1983), 602–603.
44. ———, *Singularities of the X-ray transform and limited data tomography in \mathbb{R}^2 and \mathbb{R}^3* , SIAM J. Math. Anal. **24** (1993), 1215–1225.
45. ———, *Helgason's Support Theorem and Spherical Radon Transforms*, Contemporary Mathematics (2008).
46. Eric Todd Quinto and Ozan Öktem, *Local tomography in electron microscopy*, SIAM J. Appl. Math. **68** (2008), 1282–1303.
47. D. Solmon, *The identification problem for the exponential Radon transform*, Math. Methods in the Applied Sciences **18** (1995), 687–695.
48. O. J. Tretiak and C. Metz, *The exponential Radon transform*, SIAM J. Appl. Math. **39** (1980), 341–354.
49. E.I. Vainberg, I. A. Kazak, and V. P. Kurozaev, *Reconstruction of the internal three-dimensional structure of objects based on real-time integral projections*, Soviet Journal of Nondestructive Testing **17** (1981), 415–423.
50. J-M Wagner, F. Noo, and R. Clackdoyle, *Exact Inversion of the exponential X-ray transform for rotating slant-hole (RSH) SPECT*, Phys. Med. Biol. **47** (2002), 2713–2726.
51. Y. Ye, H. Yu, and G. Wang, *Cone beam pseudo-lambda tomography*, Inverse Problems **23** (2007), 203–215.

DEPARTMENT OF MATHEMATICS, TUFTS UNIVERSITY, MEDFORD, MA 02155
E-mail address: todd.quinto@tufts.edu

DEPARTMENT OF MATHEMATICS, TUFTS UNIVERSITY, MEDFORD, MA 02155

DEPARTMENT OF MATHEMATICS, UNIVERSITY OF MICHIGAN, ANN ARBOR,
MICHIGAN